Chemical Science

ROYAL SOCIETY OF CHEMISTRY

EDGE ARTICLE

View Article Online
View Journal | View Issue

Cite this: *Chem. Sci.*, 2025, **16**, 19888

All publication charges for this article have been paid for by the Royal Society of Chemistry

Single-crystal synchrotron X-ray diffraction study reveals bulk intermediate M2 phase during the VO_2 insulator-to-metal transition

Jacob Svane, [a] Michael Anthony Quintero, [a] Emilie Skytte Vosegaard, [a] Magnus Kløve, [a] Daniel Alexander Mayoh, [b] Geetha Balakrishnan [b] and Bo Brummerstedt Iversen *[a]

Received 28th June 2025
Accepted 16th September 2025

DOI: 10.1039/d5sc04769b

rsc.li/chemical-science

The structure of solid state grown VO_2 crystals was characterized by synchrotron single crystal X-ray diffraction in the temperature region 300–355 K. Upon heating, a phase transition from the M1($P2_1/c$) phase to the R($P4_2/mnm$) phase was observed at ~341 K corresponding to the well-known insulator to metal (IMT) phase transition. Upon cooling however, the R phase proceeds first through the intermediate M2 phase between 345 and 340 K before converting to the M1 phase. This constitutes the first observation of the R → M2 → M1 phase progression in pristine free standing single crystals of VO_2, a result reported previously only in doped samples, nanocrystals, and thin films. The vanadium coordination in the M2($C2/m$) phase is found to exhibit structural characteristics of both the M1($P2_1/c$) and R($P4_2/mnm$) phases containing both V–V dimers and 1-dimensional V chains along the c-axis. The presence of the insulating M2($C2/m$) phase in undoped VO_2 is consistent with a Mott–Hubbard type IMT phase transition. Significant changes in the vanadium atomic displacement parameters observed at 340 K suggest thermal vibrations play a crucial role in the phase transition.

1. Introduction

Vanadium(IV) dioxide (VO_2) has attracted broad attention due to the reversible insulator-to-metal transition (IMT) observed around 67 °C from the rutile-like monoclinic (M1, $P2_1/c$) phase to the rutile (R, $P4_2/mnm$) phase.[1–3] The near room temperature IMT can be utilized in a range of modern applications including infrared smart windows,[4–6] infrared imaging,[7,8] field-effect transistors,[9,10] gas sensors[11] and data storage.[12] Several different polymorphs have been reported for the VO_2 system, but the IMT is only observed for the phase transition between the M1($P2_1/c$) and R($P4_2/mnm$)[13] phases. Despite decades of research and extensive discussion,[14] the mechanism behind the rapid[15] phase transition between the M1($P2_1/c$) and R($P4_2/mnm$) phases in VO_2 is still not well understood. In the R($P4_2/mnm$) phase, all vanadium atoms are equidistant (r_{eq}), while they have been found to dimerize in the M1($P2_1/c$) phase resulting in a shortening of one vanadium–vanadium distance (r_1) and an elongation of another vanadium–vanadium distance (r_2).

Two competing models are used to describe the phase transition between the M1($P2_1/c$) and R($P4_2/mnm$) phases.[16,17] The Peierls model describes the IMT as a structural distortion where the chemical bonding in the 1D chains changes from a metallic state with shared d-orbitals between all the vanadium atoms in the R($P4_2/mnm$) structure to an insulating state with localized d-orbital overlap in each vanadium–vanadium dimer in M1($P2_1/c$) structure. This is complemented by a structural change in the vanadium–vanadium distances from $r_{eq} = 2.88$ Å in the R($P4_2/mnm$) phase to $r_1 = 2.65$ Å and $r_2 = 3.12$ Å in the M1($P2_1/c$) phase.[18] The Peierls model accounts for the pico-second timeframe displacement of atoms observed using femtosecond electron diffraction[15] and is supported by the observation of soft phonon modes in the R($P4_2/mnm$) phase with inelastic X-ray and neutron scattering,[19] but fails to describe the low conductivity of the metallic R($P4_2/mnm$) phase[20] and the presence of intermediate phases.[21] The second model used to describe the IMT is the Mott–Hubbard model. In this model, the phase transition is not driven by structural changes. Instead, the structural changes are believed to be induced by changes in the electron–electron interactions which will occur when the relation $n_e^{1/3} a_H \approx 0.2$ is fulfilled, where n_e is the electron density and a_H is the Bohr radius of the valence electrons.[22] The relation sets a criterion for when the valence electron density is high enough that the electronic kinetic energy (electron hopping) overcomes the Coulomb (or Hubbard) repulsion between electrons resulting in conductivity. The Mott–Hubbard description of the IMT in VO_2 is supported by theoretical calculations including Hubbard repulsion accurately determining the band gap in M1($P2_1/c$)[23] and is not contradicted by the presence of intermediate phases.

[a]*Center for Sustainable Energy Materials, Department of Chemistry, Aarhus University, Langelandsgade 140, 8000 Aarhus, Denmark. E-mail: bo@chem.au.dk*
[b]*Department of Physics, University of Warwick, Coventry, CV4 7AL, UK*

Studies have reported an intermediate monoclinic phase (M2, $C2/m$) for samples that contain a high degree of strain *e.g.* samples of VO_2 doped with Tungsten,[24] Chromium,[25,26] Gallium,[27] Aluminum[28] and Magnesium.[29] Recently, this intermediate phase has also been observed in pure samples of VO_2 with a high degree of strain such as thin films[21,30,31] and nanocrystals grown on a mismatched lattice of sapphire.[32] The occurrence of the M2($C2/m$) phase supports the Mott–Hubbard model description of the phase transition as the M2($C2/m$) phase has been found to be insulating despite the presence of non-dimerized vanadium atoms.[33] As of today, neither of the two models has been found to unequivocally describe the IMT proving the necessity of further studies of VO_2.[20]

The R($P4_2/mnm$), M1($P2_1/c$) and M2($C2/m$) phases as projected along the [010] and [001] directions of the R($P4_2/mnm$) phase are shown in Fig. 1a and b, respectively. The R($P4_2/mnm$) phase has two chains of octahedrally coordinated vanadium atoms along the [001] direction placed at the corner and in the center of the unit cell, respectively. As can be seen in Fig. 1a, the transition between the R($P4_2/mnm$) phase and the M1($P2_1/c$) phase results in a dimerization of the vanadium atoms causing a distortion of the octahedra. The distortion of vanadium in the M1($P2_1/c$) phase is found along the [110] and [1$\bar{1}$0] direction of the R($P4_2/mnm$) phase as is evident from Fig. 1b; half along each direction. In the M2($C2/m$) phase, only half of the vanadium atoms dimerize as can be seen from Fig. 1a. Here, the atoms in one of the two vanadium chains can be seen to dimerize which gives rise to a buckling of the vanadium atoms in the other chain.

Here, we report the single crystal structure of undoped VO_2 across the phase transition during heating as well as cooling using single crystal X-ray diffraction (SCXRD) from the SPring-8 synchrotron source. The structural changes during heating and cooling are reported including accurate atomic positions and atomic displacement parameters (ADPs). We report the first direct observation of the M2($C2/m$) phase in a bulk single crystal of undoped VO_2.

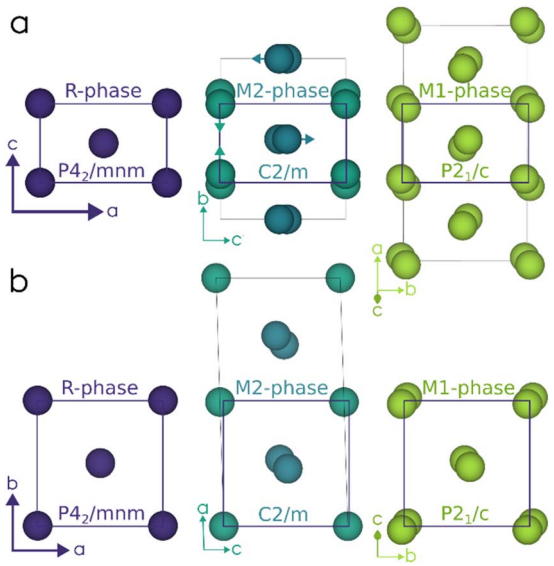

Fig. 1 Projection of the vanadium atoms in R($P4_2/mnm$), M1($P2_1/c$) and M2($C2/m$) phases as seen along the (a) [010] and (b) [001] direction the R($P4_2/mnm$) phase. The unit cell of the R($P4_2/mnm$) phase is superimposed on the M1($P2_1/c$) and M2($C2/m$) phase in both figures for easier visualization of the distortion from the high temperature setting. Arrows on atoms represent the direction of movement of the vanadium atoms from the R($P4_2/mnm$) phase to the M2($C2/m$) phase.

2. Experimental

2.1. Synthesis

Phase pure powder of M1($P2_1/c$) phase VO_2 was synthesized by reacting powder of V_2O_3 with powder of NH_4VO_3 in molar ratio 1 : 2 in argon atmosphere as reported by Mamakhel *et al.*[34] The mixed powders were sintered under argon at 750 °C for three hours. To obtain single crystals of VO_2 for SCXRD measurements, the powder was annealed under argon at 1200 °C for 12 hours. After annealing, crystals of dimension suitable for SCXRD were obtained. Many of the crystals showed significant twinning due to the phase transition from the highly symmetric rutile structure to the rutile-like monoclinic structure; generally, smaller crystals exhibited less twinning compared to larger crystals. A crystal which did not show any twinning was used for diffraction measurements.

2.2. SCXRD measurements and integration

Data was measured at the BL02B1 beamline at SPring-8 using a wavelength of 0.2463 Å. The beamline is equipped with a quarter χ goniometer, a Pilatus3 x 1 M CdTe detector, and a liquid nitrogen cryostat for temperature control. A single crystal with dimensions 45 μm × 30 μm × 25 μm was used for all data collections. Datasets were collected at a series of temperatures in the following sequence: 300 K, 325 K, 335 K, 340 K, 345 K, 350 K, 355 K, 350 K, 345 K, 340 K, 335 K, and 325 K. At each temperature, three 0–180° ω scans were collected at χ values of 0°, 25° and 45° with $2\theta = 0°$. A scan width of 0.2°/frame was used resulting in a total of 2700 frames collected for each temperature. To keep all measurements within the detector's linear range, a 600-micron Ni foil attenuator and a 0.5 s/frame exposure time were used.

The data was converted to Bruker format using the Pilatus3 frame conversion software developed by Krause.[35] Data reduction was performed in the Apex5 GUI using SAINT[36] with the recurrence background setting. Scaling and absorption correction ($\mu_r = 0.06$) of the integrated data, rejection of outliers, and estimation of uncertainties was performed in the Apex5 GUI using SADABS[37] or TWINABS[38] for single domain and twinned structures respectively. Structures were solved using SHELXT[39,40] and refined using an independent atom model in SHELXL[41] using the OLEX2 [42] GUI.

Refinement of structural models included atomic positions, anisotropic atomic displacement parameters, weighing schemes, and extinction corrections. Occupancy of the vanadium atoms were initially freely refined to check for non-stoichiometry but in all cases refined to 1 ± 0.002 suggesting full occupancy and so were fixed to 1. The resulting integration and refinement statistics can be found in Table 1. The lower

Table 1 Integration and refinement statistics. Note that the data measured at $\chi = 0°$ at 345 K during cooling was integrated and solved in the R($P4_2/mnm$) phase while the data measured at $\chi = 25°$, 45° at 345 K during cooling was integrated and solved in the M2($C2/m$) phase

	Space group, measured reflections (twin fractions %)	Reflections $I > 3\sigma$, unique reflections	Resolution[a] (Å^{-1}), redundancy, completeness (%)	Rint, $R\sigma$, I/σ	R_1, wR_2, GOF	Highest peak and deepest hole
300 K	$P2_1/c$, 11 607	10 238, 1077	0.5, 10.33, 98.9	0.0525, 0.0236, 42.3	0.0449, 0.1349, 1.459	2.197, −2.945
325 K heating	$P2_1/c$, 11 582	9785, 1070	0.5, 9.96, 98.2	0.0523, 0.0243, 41.1	0.0496, 0.1470, 1.430	2.161, −3.087
335 K heating	$P2_1/c$, 11 646	9979, 1080	0.5, 10.04, 99.0	0.0632, 0.0288, 34.7	0.0512, 0.1420, 1.452	2.129, −2.753
340 K heating	$P2_1/c$, 11 587	7588, 1074	0.5, 7.70, 98.4	0.0731, 0.0420, 23.8	0.0698, 0.1656, 1.140	2.106, −2.382
345 K heating	$P4_2/mnm$, 5752	4926, 181	0.5, 31.53, 100	0.0518, 0.0166, 60.2	0.0109, 0.0296, 1.300	0.270, −0.351
350 K heating	$P4_2/mnm$, 5783	5006, 179	0.5, 32.17, 100	0.0515, 0.0168, 59.4	0.0113, 0.0309, 1.296	0.278, −0.334
355 K heating	$P4_2/mnm$, 5715	5151, 180	0.5, 33.02, 100	0.0514, 0.0158, 63.2	0.0102, 0.0267, 1.318	0.282, −0.374
350 K cooling	$P4_2/mnm$, 5793	5217, 182	0.5, 33.09, 100	0.0523, 0.0158, 63.4	0.0108, 0.0285, 1.385	0.336, −0.337
345 K cooling ($\chi = 0°$)	$P4_2/mnm$, 4040	3345, 146	0.5, 10.51, 96.8	0.0539, 0.0306, 32.7	0.0166, 0.0377, 1.147	0.459, −0.462
345 K cooling ($\chi = 25°$, 45°)	$C2/m$, 17 831 (87.45(10), 3.14(4), 9.41(9))	16 052, 2556	0.5, 3.17, 99.6	0.0766, 0.0363, 27.6	0.0492, 0.1434, 1.127	2.322, −2.248
340 K cooling	$C2/m$, 26 537 (84.9(9), 4.1(8) and 11.0(3))	23 832, 2705	0.5, 2.03, 98.2	0.0940, 0.0361, 27.7	0.0345, 0.1501, 1.288	1.999, −3.166
335 K cooling	$P2_1/c$, 17 396 (84.0(5), 16.0(5))	14 620, 2302	0.5, 2.36, 99.4	0.0977, 0.0548, 18.3	0.0552, 0.1727, 1.111	2.950, −2.570
325 K cooling	$P2_1/c$, 15 445 (84.78(14), 15.22(14))	15 239, 2525	0.5, 3.45, 100	0.0955, 0.0500, 20.0	0.0398, 0.1090, 1.242	1.816, −1.366

[a] Resolution was cut at 0.5 Å^{-1} for all datasets due to scattering from the attenuator at higher resolution.

symmetry of the M1($P2_1/c$) and M2($C2/m$) phases compared to the R($P4_2/mnm$) phase justify the larger features in the residuals observed for these phases. Anharmonic thermal displacement parameters were refined but were not significant within two standard deviations and were therefore not included in the models. The low temperature phase formed during cooling turned out to be twinned and so a twin law was applied combined with a twin fraction refinement. Inductively Coupled Plasma Optical Emission Spectroscopy (ICP-OES) was used to confirm that the sample contained no unintentional doping; the resulting molar percentages from the measurement can be found in the SI (Table S1) along with the methodology.

3. Results and discussion

3.1. Phase identification

3.1.1. General remarks. Due to the difference in space group symmetry and unit cell parameters the tetragonal phase has significantly fewer Bragg reflections than the monoclinic phases. By visual inspection of the raw data frames (aided by an overlay of the possible space groups), it was possible to identify the instantaneous reversible phase transition during some of the datasets.

3.1.2. Heating and cooling. The M1($P2_1/c$) phase was observed at 300 K and persisted upon heating through 325 K and 335 K. At 340 K the crystal fluctuated between the M1($P2_1/c$) and R($P4_2/mnm$) phases throughout the data collection, the reasons for which are discussed further below. Only the R($P4_2/mnm$) phase was observed for the rest of the heating sequence at 345 K, 350 K, and 355 K as well as into the cooling sequence at 350 K. Upon cooling to 345 K, the M2($C2/m$) phase was observed over frames 1–36, 708, and 709 with the R($P4_2/mnm$) phase being observed for the rest of the collection. At 340 K only the M2($C2/m$) phase was observed. Upon cooling to 335 K and 325 K only the M1($P2_1/c$) phase was observed.

3.1.3. Oscillatory behavior. Oscillatory phase transitions were observed during isothermal data collections at 340 K (heating) and 345 K (cooling), these temperatures being in the vicinity of the reported 1st order phase transition at 341 K.[1–3] Furthermore, they were observed only during ω scans collected with $\chi = 0°$, whereas scans collected with $\chi = 25°$ and 45° contained only one phase. For the 340 K (heating) dataset the R($P4_2/mnm$) phase is observed in 86 out of the total 900 frames while in the rest only the M1($P2_1/c$) phase is present. These frames are divided into eight instances which are evenly distributed throughout the collection and vary in length from 1 to 23 sequential observations, representative frames are depicted in Fig. S1.

The per-frame correlation coefficient, <Corr>, output from SAINT is a measure of the degree of per-frame agreement with the integration parameters for a given cell. For high quality data <Corr> typically falls between 0.6 and 1.0, with lower correlations indicating significant disagreements. A comparison of the <Corr> coefficients for the $\chi = 0°$ run at 340 K when integrated with both the R($P4_2/mnm$) and M1($P2_1/c$) phases, see Fig. S2(a) and (b), shows that when <Corr> is low for R($P4_2/mnm$), it is high for M1($P2_1/c$) and *vice versa*. This result confirms the switching behavior suggested from visual inspection of the data. In the case of the 345 K (cooling) dataset, the M2($C2/m$) phase is observed on frames 1–36, 708, and 709 while the R($P4_2/mnm$) phase is observed on the rest, see Fig. S3. Collectively, these observations imply the existence of some temperature instability during the data collections.

Table 2 Unit cell parameters from SCXRD refinement. Note that the data measured at 345 K while cooling at $\chi = 0°$ was found to be the R($P4_2/mnm$) phase while the data measured at $\chi = 25°$, 45° was found to be the M2($C2/m$) phase

	Space group	Phase	a [Å]	b [Å]	c [Å]	β°	Volume [Å^3]/# V atoms in unit cell
300 K	$P2_1/c$	M1	5.7591(4)	4.5313(4)	5.3914(4)	122.6005(13)	118.528(16)/2
325 K heating	$P2_1/c$	M1	5.7614(4)	4.5318(3)	5.3924(4)	122.6081(13)	118.601(14)/2
335 K heating	$P2_1/c$	M1	5.7654(5)	4.5344(4)	5.3958(4)	122.6148(15)	118.817(17)/2
340 K heating	$P2_1/c$	M1	5.7554(9)	4.5235(7)	5.3828(8)	122.602(3)	118.06(3)/2
345 K heating	$P4_2/mnm$	R	4.5675(5)	4.5675(5)	2.8577(3)	90	59.617(14)/1
350 K heating	$P4_2/mnm$	R	4.5627(5)	4.5627(5)	2.8552(3)	90	59.44(14)/1
355 K heating	$P4_2/mnm$	R	4.5556(5)	4.5556(5)	2.8513(3)	90	59.174(14)/1
350 K cooling	$P4_2/mnm$	R	4.5613(5)	4.5613(5)	2.8544(3)	90	59.387(14)/1
345 K cooling ($\chi = 0°$)	$P4_2/mnm$	R	4.5680(9)	4.5680(9)	2.8573(6)	90	59.62(3)/1
345 K cooling ($\chi = 25°$, 45°)	$C2/m$	M2	9.0684(8)	5.8097(5)	4.5297(4)	91.7911(17)	238.53(4)/4
340 K cooling	$C2/m$	M2	9.0678(6)	5.8077(4)	4.5288(3)	91.7895(15)	238.38(3)/4
335 K cooling	$P2_1/c$	M1	5.7637(5)	4.5351(5)	5.3908(6)	122.6056(18)	118.70(2)/2
325 K cooling	$P2_1/c$	M1	5.7593(5)	4.5321(4)	5.3881(5)	122.6164(14)	118.460(18)/2

Given that phase transitions were observed only with $\chi = 0°$ (vertical alignment of goniometer head) it is likely that this position produces a slightly higher temperature compared to the other χ positions. This fact, combined with fluctuations in the cryostream is sufficient to explain the observed behavior. No distinct evidence of a phase transition, such as large drops in intensity, was observed in any of the recorded frames suggesting that the speed of the phase transition falls well below the 0.5 s exposure time used. This result is consistent with studies reporting the timescale of the transitions to be on the order of femto-to-picoseconds.[15,43] Based on the concerted nature of the phase transition in VO_2 at 341 K during heating[1–3] we estimate that the temperature fluctuated ~1–2 K during our experiments.

The M1($P2_1/c$) and M2($C2/m$) phases during cooling were found to contain twin domains. In the M1($P2_1/c$) phase at 335 K and 325 K during cooling one twin domain was observed with the major component comprising 84.0(5)% and 84.78(14)% in the two datasets respectively. In the M2($C2/m$) phase three domains were observed. For the data measured at 345 K during cooling the three domains constituted 87.45(10)%, 3.14(4)% and 9.41(9)% respectively while the three domains in the data measured at 340 K during cooling constituted 84.9(9)%, 4.1(8)% and 11.0(3)% respectively. For all four datasets, the major twin component was thus found to make up ~85% of the crystal. The phase transition temperature from the M1($P2_1/c$) phase to the R($P4_2/mnm$) phase was found to happen during the measurement at 340 K during heating corresponding well to earlier reported values obtained from measurements of the optical properties and resistivity measurements of 341 K.[44,45] The phase transition from the R($P4_2/mnm$) phase to the M2($C2/m$) phase has only been observed in thin films of phase pure VO_2 and is found to occur around 345 K. The phase transition between the M2($C2/m$) and M1($P2_1/c$) phase is typically observed between 340 K and 335 K during cooling.

3.2. Structure

3.2.1. Geometry of the M1/R phase transition. The refined unit cell parameters can be found in Table 2 along with the space group of the structure. The unit cell parameters of the M1($P2_1/c$)[46] and R($P4_2/mnm$)[47] phases are found to be similar to those reported earlier; the unit cell parameters of the M2($C2/m$) phase are likewise similar to earlier reports on the Cr doped VO_2.[48] It is found that the unit cell volume of the M1($P2_1/c$) phase increases during heating until 340 K at which point the volume decreases. The decrease in unit cell size is observed when integrating the data measured at all three χ angles and when integrating only the data measured at $\chi = 25°$ and $\chi = 45°$ where M1($P2_1/c$) is the only observed phase. The refined unit cell parameters normalized by the number of vanadium atoms in the unit cell can be seen in Fig. 2. Along with this decrease in volume a decrease is observed in the V–V distance and the V–O distances. The V–O distances are found to be constant within uncertainty during the heating until 340 K while the V–V distances increase. The average V–O bond length at 300 K, 325 K and 335 K during the heating is found to be 1.940(3) Å, 1.940(3) Å and 1.941(3) Å respectively. At 340 K, the average bond length decreases to 1.937(3) Å suggesting a shift towards the higher symmetry R($P4_2/mnm$) phase which is found to have an average V–O bond length of 1.930(3) Å at 345 K. The V–V–V angles are found to increase during heating moving toward the linear setting observed in the R($P4_2/mnm$) phase. The octahedra in the M1($P2_1/c$) phase has three short bonds and three longer bonds placed in a *fac* configuration. In the R($P4_2/mnm$) phase, the octahedra has two long bonds in the axial position and four short bonds in the equatorial plane. The distortion of the octahedra has been estimated using OctaDist[49] where the parameters Σ and Θ describe the summed angular deviation from a perfect octahedra and the distortion from a perfect octahedral to a trigonal prismatic geometry; a number closer to zero indicate a more perfect octahedral coordination. Selected bond distances, angles between vanadium atoms, distortion parameters calculated using OctaDist and atomic displacement parameters (ADPs) can be found in Table S2 in the SI. The angular deviation decreases from 57.1° to 56.1° in the M1($P2_1/c$) phase during the heating before dropping to 23.3° in the R($P4_2/mnm$) phase. Similarly, Θ is found to decrease (122.3°–121.5°) with increasing temperature before decreasing to 107.7°. Despite the changes being small, both these parameters suggest

a shift toward higher symmetry as the temperature is increased. After the phase transition to the R($P4_2/mnm$) phase Σ and Θ decrease significantly indicating a transition to a less distorted octahedra. Despite the large shift in the values, the octahedra are still found to exhibit some degree of distortion; no significant change is observed in the distortion of the octahedra during further heating of the crystal after the transition to the R($P4_2/mnm$) phase. The V–O and V–V distances decrease with increasing temperature in the R($P4_2/mnm$) phase resulting in a decrease in the unit cell volume. After the phase transition reversing to the M1($P2_1/c$) phase during cooling, the V–V distances, the V–O distances, the V–V–V angles and the calculated distortion parameters show the same trend of increasing distortion further away from the phase transition temperature.

3.2.2. The M2 phase. After the phase transition from the R($P4_2/mnm$) phase to the M2($C2/m$) phase upon cooling, two different octahedral coordination environments are observed for vanadium; these will be discussed as the distorted ($M2_{M1}$) and non-distorted ($M2_R$) octahedral, with the symmetry referring to the pseudo symmetry present in the M1($P2_1/c$) and R($P4_2/mnm$) phases, respectively. This naming convention is given in relation to the projection along the [001] direction of the R($P4_2/mnm$) phase as seen in Fig. 1 where the vanadium atoms in the corners do not distort while the vanadium atoms in center of the center are distorted compared to the R($P4_2/mnm$) phase. The V–O distances in the distorted octahedra have the same distribution as the $M2_{M1}$ octahedra of the M1($P2_1/c$) phase with three short bonds and three longer bonds, while the non-distorted $M2_R$ octahedra have two long bonds and four short bonds, similar to what is observed in the R($P4_2/mnm$) phase. The $M2_{M1}$ vanadium atoms in the M2($C2/m$) phase undergo dimerization reducing the bond length by 0.3 Å akin to what is observed in the M1($P2_1/c$) phase. The V–V distance between $M2_R$ vanadium atoms is found to increase by ~0.08 Å after the phase transition from R($P4_2/mnm$) to the M2($C2/m$) phase. The distances between the dimerized vanadium atoms in M2($C2/m$) are found to differ from the distances observed in the M1($P2_1/c$) phase by ±0.1 Å with the short distance decreasing by ~0.1 Å and the long distance increasing by ~0.1 Å. The V–V–V angles of the vanadium atoms in M2($C2/m$) for the $M2_{M1}$ octahedra are found to differ from the V–V–V angles in the M1($P2_1/c$) phase with the angle along the [001] projection of the R($P4_2/mnm$) phase being ~5° smaller and the angle along the [010] projection of the R($P4_2/mnm$) phase being ~1° larger compared to the M1($P2_1/c$) phase. The angle along the [001] projection of the R($P4_2/mnm$) phase in the non-distorted octahedra is found to be 180° as for the R($P4_2/mnm$) phase while the angle along the [010] projection is found to be ~1° smaller than the corresponding angle in the M1($P2_1/c$) phase. The average of the V–V–V angles in the M2($C2/m$) phase as seen down the [010] projection of the R($P4_2/mnm$) phase are found to be 171.76(3)° at 340 K during cooling which, within the uncertainty, is the same angle found for the M1($P2_1/c$) phase in the data measured at 340 K during heating. This corroborates the observation that the M1($P2_1/c$) phase can be seen as a superposition of two orthogonal M2($C2/m$) networks.[50] An illustration of the four different octahedra can be found in

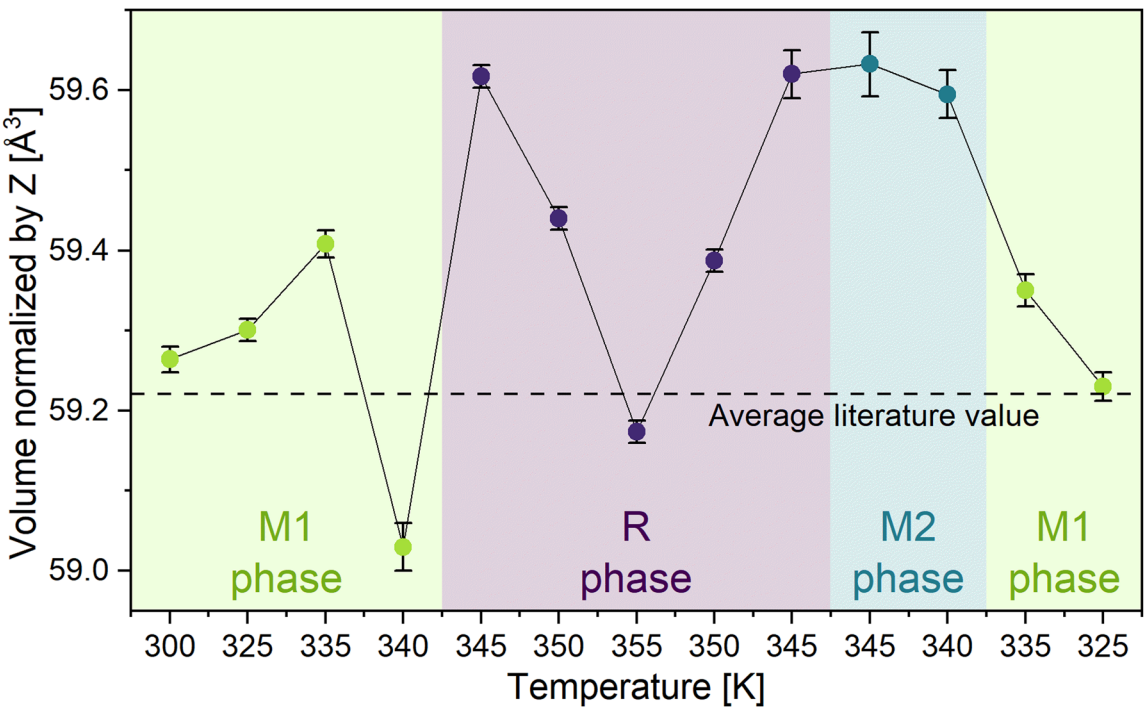

Fig. 2 Volume of unit cell normalized by number of vanadium atoms in the unit cell as a function of temperature. Green shaded areas show temperatures where the M1($P2_1/c$) phase is found, purple shaded areas show temperatures where the R($P4_2/mnm$) phase is found, and blue shaded areas show temperatures where the M2($C2/m$) phase is found. Average literature values extracted from the ICSD for the M1($P2_1/c$), M2($C2/m$), and R($P4_2/mnm$) phases.

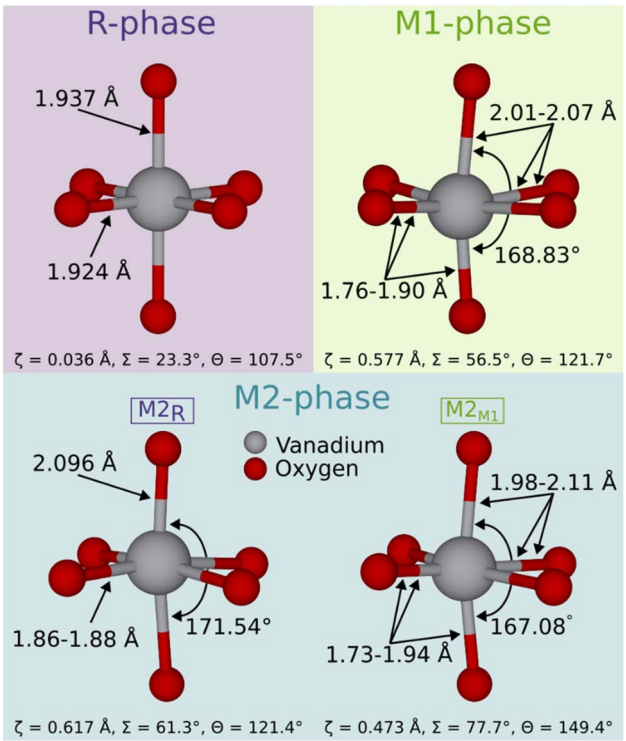

Fig. 3 Coordination of vanadium for the R($P4_2/mnm$), M2($C2/m$) and M1($P2_1/c$) phases. The M2($C2/m$) phase vanadium coordinated in a pseudosymmetry of $M2_R$ is seen on the left while the vanadium coordinated in a pseudosymmetry of $M2_{M1}$ can be seen on the right.

Fig. 3. Looking at the calculated distortion parameters for the M2($C2/m$) phase it is found that the distorted octahedra are deviating more from the perfect octahedral geometry compared to the octahedra observed in the M1($P2_1/c$) and R($P4_2/mnm$) phases. The $M2_{M1}$ and $M2_R$ octahedra in the M2($C2/m$) phase have Θ values 30° or 15° higher than the corresponding octahedral in the M1($P2_1/c$) and R($P4_2/mnm$) phases, while the Σ values are found to be ~40° and ~20° larger.

The observation of the M2($C2/m$) phase in a free-standing bulk crystal establishes the M2 intermediate phase as intrinsic to VO_2. Given that the M2($C2/m$) phase is insulating with chains of vanadium atoms present in the structure, the presence of the M2($C2/m$) phase has been previously interpreted as indicative of a Mott–Hubbard mechanism in VO_2.[33] Altogether, these results establish the M2($C2/m$) phase as an intrinsic part of the VO_2 phase diagram and strongly support that a Mott–Hubbard mechanism underlies the insulator–metal transition.

3.2.3. Atomic displacements parameters. The obtained anisotropic ADPs along the principal axes for vanadium are plotted in Fig. 4A–C along with the calculated equivalent isotropic ADPs (Fig. 4D) for all temperatures; the M1($P2_1/c$) and R($P4_2/mnm$) phases are shown as circles and the M2($C2/m$) phase is shown as upwards and downwards pointing triangles for the distorted ($M2_{M1}$) and non-distorted ($M2_R$) vanadium atoms respectively. All anisotropic ADPs for vanadium can be found in Fig. S4. Looking first at the equivalent isotropic ADP, U_{eq}, it can be seen that the increase in temperature from 300 K to 340 K results in an increase of the ADPs for the M1($P2_1/c$) phase and that the equivalent isotropic ADPs for the M2($C2/m$) and M1($P2_1/c$) phases upon cooling are similar to these. The isotropic ADPs for the M1($P2_1/c$) and M2($C2/m$) phases are found to be comparable to earlier reported values.[48,51] Furthermore, it is observed that the isotropic ADPs for the R($P4_2/mnm$) phase are close to twice as large as those found for the M1($P2_1/c$) and M2($C2/m$) phases, even the M2($C2/m$) phase observed at the same temperature. This complements values reported for both Cr doped VO_2 (ref. 48) and pure VO_2 in the R($P4_2/mnm$) phase.[47] The ADPs for the R($P4_2/mnm$) phase are abnormally high compared to those of other rutile structures[52] and have been suggested to play a role in the MIT.[47]

Looking at the principal axis anisotropic ADPs for vanadium (U_{11}, U_{22}, U_{33}) in Fig. 4A–C and Table S2 for the M1($P2_1/c$) phase it can be seen that the displacement along the U_{33} direction increases by ~0.001 Å^2 at from 335 K to 340 K during heating while U_{22} increase ~0.0005 Å^2 and U_{11} decrease by ~0.0003 Å^2. At temperatures below 340 K, the displacement of vanadium is observed to be almost parallel to the body diagonal of the unit cell of the M1($P2_1/c$) phase while the displacement at 340 K during heating is close to being perpendicular to the *ab*-plane of the M1($P2_1/c$) phase. This change corresponds to an elongation of the displacement parameters towards the observed position of vanadium in the R($P4_2/mnm$) phase. The displacement direction of vanadium is illustrated in Fig. 5 for all the measured temperatures. The ADPs of oxygen at 340 K are found keep the orientation from the data measured at 335 K with only small change in size being observed. From this it can be inferred that the phase change is caused by displacement of the vanadium. The position of vanadium is found to be shifting small amounts throughout the heating from 300 K to 340 K. The largest positional change is found to be for the *y* position going from 2.36167(11) Å to 2.35308(12) Å. The *x* and *z* parameters change from 1.30409(10) Å to 1.30385(10) Å and 0.11981(10) Å to 0.11758(12) Å respectively. The displacement in the *y* position of the vanadium atom correspond to a shift toward the higher symmetry position which vanadium occupy in the R($P4_2/mnm$) phase. Upon cooling the same phenomenon is observed after the transition from the M2($C2/m$) to the M1($P2_1/c$) phase where U_{33} for the vanadium in the M1($P2_1/c$) phase at 335 K during cooling is found to be ~0.002 Å^2 larger than the U_{33} for the M1($P2_1/c$) phase at 325 K during cooling.

The shift in the displacement direction of the vanadium atoms close to the phase transition can be used to explain earlier reported Raman spectra where it has been observed that some phonon modes differ greatly in behavior. For VO_2 thin films, it has been reported that the A_g modes and B_g modes behave differently during heating. For the A_g peak at 618 cm^{-1} the peak intensity decreases continuously while the B_g peak at 825 cm^{-1} does not undergo significant change with heating until 340 K where it suddenly disappears.[53] This sudden change in peak intensity can be correlated with the observed change in the ADPs observed for V at 340 K during heating which can be observed in Fig. 5. Here it is evident that the displacement of vanadium undergoes a large change in direction between 335 K

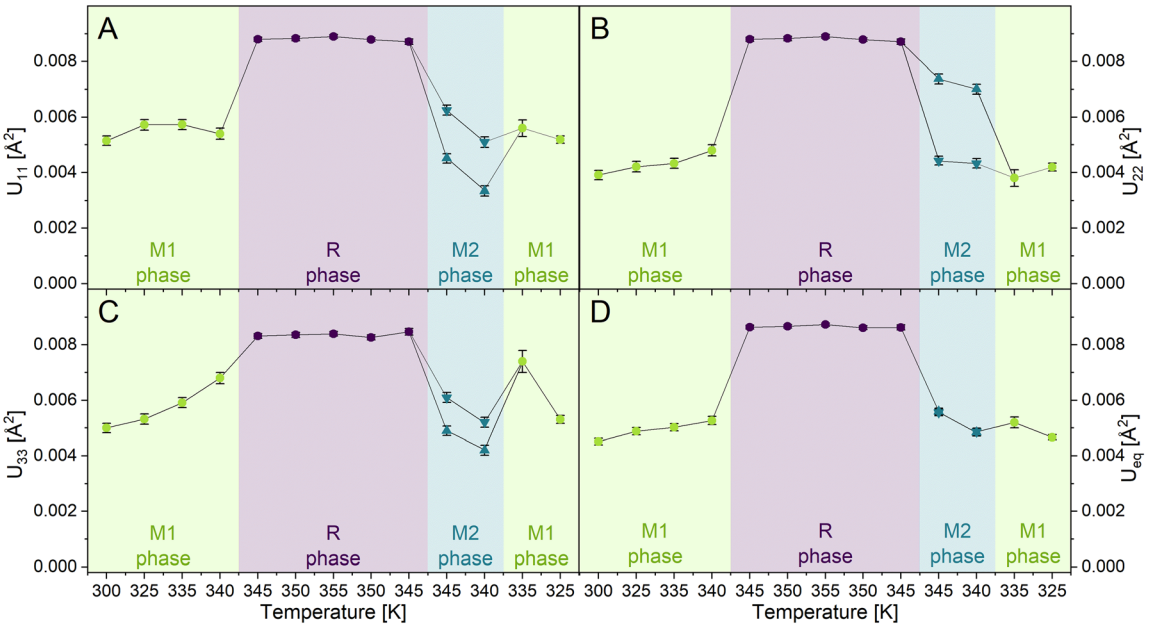

Fig. 4 Anisotropic atomic displacement parameters U_{11}(A), U_{22}(B), U_{33}(C), and equivalent isotropic atomic displacement parameters ($U_{eq} = (U_{11} + U_{22} + U_{33})/3$) (D) for vanadium atoms at all temperatures. The distorted ($M2_{M1}$) and non-distorted ($M2_R$) vanadium atoms in the M2($C2/m$) phase are represented by a triangle pointing up and down respectively. Uncertainties are included in the figure but obscured by the tick marks.

and 340 K which can explain the change in symmetry and therefore energy of the vibration observed in the Raman spectrum. Furthermore, from Fig. 5 it is evident that the atomic displacement of vanadium in the M1($P2_1/c$) phase is not along a specific bond. Instead, the vibration is found to be in the direction towards the vanadium–vanadium dimer.

The ADPs of the two different vanadium atoms in the M2($C2/m$) phase are found to be dissimilar. The $M2_R$ vanadium at 340 K during cooling is found to have similar ADPs along all three principal axes with $U_{11,M2}$ and $U_{33,M2}$ being 0.00510(19) Å^2 and 0.00521(18) Å^2 respectively while $U_{22,M2}$ is found to be 0.00433(17) Å^2. This distribution is not unlike what is found in

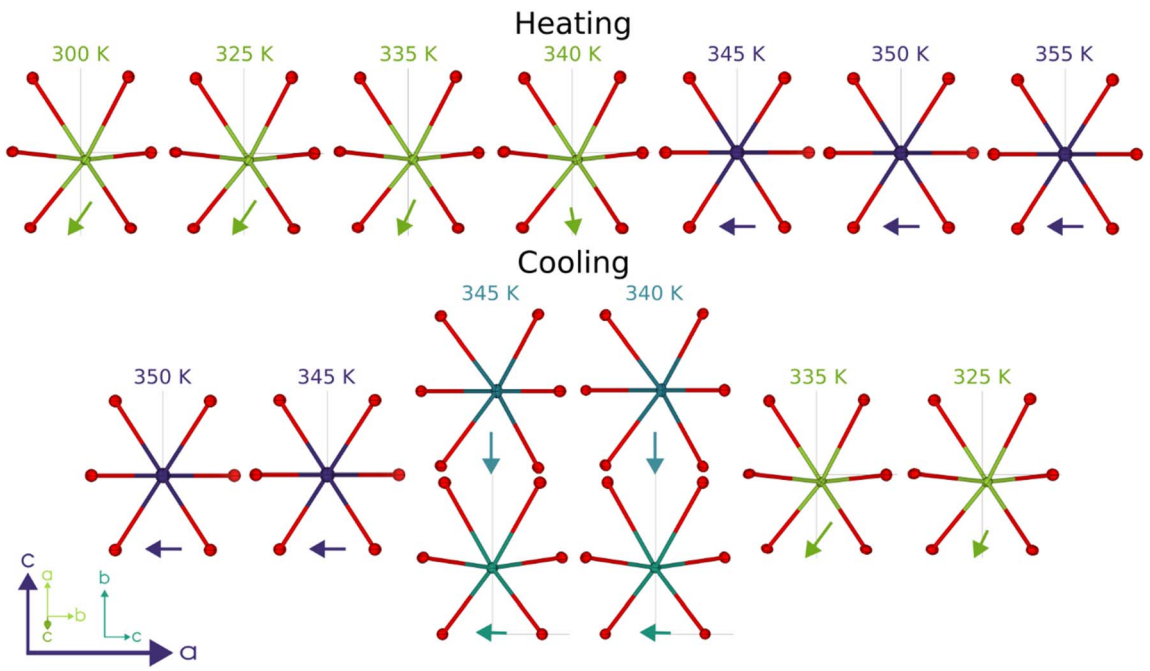

Fig. 5 Direction of atomic displacement of vanadium in octahedral coordination at all temperatures along with projections of the direction of the largest displacement magnitude of vanadium. Displacements are plotted as 50% probability. All temperatures are plotted in the same projection as Fig. 1a corresponding to the ac-plane of the R($P4_2/mnm$) phase.

the R($P4_2/mnm$) phase where two of the ADPs ($U_{11,R} = U_{22,R} =$ 0.00890(7) Å^2 at 355 K) along the principal axes are found to be equal while the third ($U_{33,R} = 0.00840(8)$ Å^2 at 355 K) is found to be smaller. From the projection of the M2($C2/m$) phase on the R($P4_2/mnm$) phase (Fig. 1) it is evident that $U_{11,R} = U_{33,M2}$, $U_{22,R} \approx U_{11,M2}$, and $U_{33,R} = U_{22,M2}$. Thus the direction of the displacement of the $M2_R$ vanadium in the M2($C2/m$) phase is found to be identical with the vanadium in the R($P4_2/mnm$) phase. The displacement parameters for the $M2_{M1}$ vanadium are found to be similar to those of the M1($P2_1/c$) phase. For the $M2_{M1}$ vanadium in the M2($C2/m$) phase, two of the ADPs ($U_{11,M2} = U_{22,R} = 0.00334(18)$ Å^2 and $U_{33,M2} = U_{11,R} = 0.00420(18)$ Å^2) along the principal axes are smaller than the third ($U_{22,M2} = U_{33,R} = 0.00701(18)$ Å^2). The displacement of the vanadium in the M1($P2_1/c$) phase as projected in the R($P4_2/mnm$) phase is found to be $U_{11,M1} = U_{33,R} = 0.00515(17)$ Å^2, $U_{22,M1} = U_{11,R} = 0.00391(17)$ Å^2, and $U_{33,M1} = U_{22,R} = 0.00397(17)$ Å^2. As with the bond distances and angles described earlier, the ADPs of the vanadium atoms in the M1($P2_1/c$) and the $M2_{M1}$ of the M2($C2/m$) phases are found to show similar behaviour. For both the vanadium in M1($P2_1/c$) and the $M2_{M1}$ vanadium in M2($C2/m$), one of the ADPs ($U_{11,M1} = U_{22,M2} = U_{33,R}$) is found to be larger compared to the two other.

4. Conclusions

We have carried out the first single crystal X-ray diffraction study of a pure VO_2 phase across the insulator–metal transition during heating and cooling. Upon heating the room temperature M1($P2_1/c$) phase changes to the R($P4_2/mnm$) at ~341 K, but during cooling from 355 K the crystal proceeds through an intermediate M2($C2/m$) phase at 345–340 K, which has previously only been reported in doped samples, nanocrystals, and thin films. We have shown that structural motifs from both the R($P4_2/mnm$) and M1($P2_1/c$) phases are present in the M2($C2/m$) phase. The vanadium atoms in M2($C2/m$) which are not dimerized show ADPs resembling those of the R($P4_2/mnm$) phase in shape while the vanadium atoms which are dimerized show ADPs resembling those of the M1($P2_1/c$) phase. The detailed analysis of the ADPs over the temperature range from 300 K to 355 K reported here supports previous studies emphasizing the important role of the change of direction of the ADPs in the phase transition.[33,54] In particular, the shift in direction of the ADPs of vanadium at 340 K immediately before the phase transition is evidence that the thermal displacement of vanadium is sensitive to the phase transition. The observation of a sequential R → M2 → M1 polymorphic phase evolution in a free-standing bulk crystal establishes the M2 intermediate phase as intrinsic to VO_2. Given that the M2($C2/m$) phase is insulating even in the absence of complete vanadium dimerization, its presence has been previously interpreted as indicative of a Mott–Hubbard mechanism in VO_2.[33] Altogether, these results establish the M2($C2/m$) phase as component of the VO_2 phase diagram in undoped bulk crystals and strongly support that a Mott–Hubbard mechanism underlies the insulator–metal transition.

Author contributions

J. S. carried out crystal synthesis, collected and analysed the SCXRD data and wrote the initial manuscript. M. A. Q. carried out data collection and data analysis and contributed to the manuscript drafts and revisions. E. S. V. carried out data analysis and contributed to the manuscript drafts and revisions. M. K. carried out data analysis and contributed to the manuscript drafts and revisions. D. A. M. carried out crystal synthesis and contributed to the manuscript drafts and revision. G. B. supervised experiments, obtained funding and edited the manuscript. B. B. I. conceptualized the study, supervised experiments and analyses, obtained funding and edited the manuscript. All authors have given approval to the final version of the manuscript.

Conflicts of interest

The authors declare no conflict of interest.

Data availability

The data that support the findings of this study are available from the corresponding author upon reasonable request.

CCDC 2440825–2440837 contain the supplementary crystallographic data for this paper.[55a–m]

Supplementary information is available. See DOI: https://doi.org/10.1039/d5sc04769b.

Acknowledgements

The work was supported by the Villum Foundation (25861), the Carlsberg Foundation, the Novo Nordisk Foundation, the Independent Research Fund Denmark and the Danish National Research Foundation (DNRF189). This work was supported by the Japan Society for the Promotion of Science (JSPS) Grants-in-Aid for Scientific Research (KAKENHI) Grant Number JP19KK0132, JP20H4656, and JP2105235. The synchrotron experiments were performed at SPring-8 BL02B1 with the approval of the Japan Synchrotron Radiation Research Institute (JASRI) (Proposals no. 2018b0078, no. 2019a0159 and no. 2021a1744).

References

1 N. B. Aetukuri, A. X. Gray, M. Drouard, M. Cossale, L. Gao, A. H. Reid, R. Kukreja, H. Ohldag, C. A. Jenkins, E. Arenholz, K. P. Roche, H. A. Dürr, M. G. Samant and S. S. P. Parkin, *Nat. Phys.*, 2013, **9**, 661–666.
2 C. N. Berglund and H. J. Guggenheim, *Phys. Rev.*, 1969, **185**, 1022.
3 T. Yao, L. Liu, C. Xiao, X. D. Zhang, Q. H. Liu, S. Q. Wei and Y. Xie, *Angew Chem. Int. Ed. Engl.*, 2013, **52**, 7554–7558.
4 Y. F. Gao, H. J. Luo, Z. T. Zhang, L. T. Kang, Z. Chen, J. Du, M. Kanehira and C. X. Cao, *Nano Energy*, 2012, **1**, 221–246.
5 S. Liang, Q. W. Shi, H. F. Zhu, B. Peng and W. X. Huang, *ACS Omega*, 2016, **1**, 1139–1148.

6 J. D. Zhou, Y. F. Gao, Z. T. Zhang, H. J. Luo, C. X. Cao, Z. Chen, L. Dai and X. L. Liu, *Sci. Rep.*, 2013, **3**, 3029.
7 C. H. Chen, X. J. Yi, X. R. Zhao and B. F. Xiong, *Sens. Actuators, A*, 2001, **90**, 212–214.
8 M. A. Richardson and J. A. Coath, *Opt. Laser Technol.*, 1998, **30**, 137–140.
9 M. Nakano, K. Shibuya, D. Okuyama, T. Hatano, S. Ono, M. Kawasaki, Y. Iwasa and Y. Tokura, *Nature*, 2012, **487**, 459–462.
10 N. Shukla, A. V. Thathachary, A. Agrawal, H. Paik, A. Aziz, D. G. Schlom, S. K. Gupta, R. Engel-Herbert and S. Datta, *Nat. Commun.*, 2015, **6**, 7812.
11 E. Strelcov, Y. Lilach and A. Kolmakov, *Nano Lett.*, 2009, **9**, 2322–2326.
12 I. Balberg and S. Trokman, *J. Appl. Phys.*, 1975, **46**, 2111–2119.
13 C. X. Cao, Y. F. Gao and H. J. Luo, *J. Phys. Chem. C*, 2008, **112**, 18810–18814.
14 J. P. Pouget, *C. R. Phys.*, 2021, **22**, 37–87.
15 P. Baum, D. S. Yang and A. H. Zewail, *Science*, 2007, **318**, 788–792.
16 Z. W. Shao, X. Cao, H. J. Luo and P. Jin, *NPG Asia Mater.*, 2018, **10**, 581–605.
17 R. M. Wentzcovitch, W. W. Schulz and P. B. Allen, *Phys. Rev. Lett.*, 1994, **72**, 3389–3392.
18 C. Z. Wu, F. Feng and Y. Xie, *Chem. Soc. Rev.*, 2013, **42**, 5157–5183.
19 J. D. Budai, J. W. Hong, M. E. Manley, E. D. Specht, C. W. Li, J. Z. Tischler, D. L. Abernathy, A. H. Said, B. M. Leu, L. A. Boatner, R. J. McQueeney and O. Delaire, *Nature*, 2014, **515**, 535.
20 P. Hu, P. Hu, T. D. Vu, M. Li, S. C. Wang, Y. J. Ke, X. T. Zeng, L. Q. Mai and Y. Long, *Chem. Rev.*, 2023, **123**, 4353–4415.
21 J. M. Atkin, S. Berweger, E. K. Chavez, M. B. Raschke, J. B. Cao, W. Fan and J. Q. Wu, *Phys. Rev. B:Condens. Matter Mater. Phys.*, 2012, **85**, 020101.
22 N. F. Mott, *Rev. Mod. Phys.*, 1968, **40**, 677.
23 V. Eyert, *Phys. Rev. Lett.*, 2011, **107**, 016401.
24 A. Boontan, E. K. Barimah, P. Steenson and G. Jose, *ACS Appl. Mater. Interfaces*, 2023, **15**, 51606–51616.
25 J. P. Pouget, H. Launois, T. M. Rice, P. Dernier, A. Gossard, G. Villeneuve and P. Hagenmuller, *Phys. Rev. B*, 1974, **10**, 1801–1815.
26 A. O. Suleiman, S. Mansouri, J. Margot and M. Chaker, *Appl. Surf. Sci.*, 2022, **571**, 151267.
27 W. Bruckner, U. Gerlach, W. Moldenhauer, H. P. Bruckner, N. Mattern, H. Oppermann and E. Wolf, *Phys. Status Solidi A*, 1976, **38**, 93–102.
28 M. Ghedira, H. Vincent, M. Marezio and J. C. Launay, *J. Solid State Chem.*, 1977, **22**, 423–438.
29 R. Basu, V. Srihari, M. Sardar, S. K. Srivastava, S. Bera and S. Dhara, *Sci. Rep.*, 2020, **10**, 1977.
30 Y. Bleu, F. Bourquard, K. Misdanitis, A. Poulet, A. S. Loir, F. Garrelie and C. Donnet, *Mater. Today Commun.*, 2023, **35**, 105564.
31 B. Hu, Y. Ding, W. Chen, D. Kulkarni, Y. Shen, V. V. Tsukruk and Z. L. Wang, *Adv. Mater.*, 2010, **22**, 5134.
32 M. Newton, U. Wagner and C. Rau, *Appl. Phys. Express*, 2022, **15**, 077001.
33 H. Kim, T. V. Slusar, D. Wulferding, I. Yang, J. C. Cho, M. Lee, H. C. Choi, Y. H. Jeong, H. T. Kim and J. Kim, *Appl. Phys. Lett.*, 2016, **109**, 233104.
34 A. Mamakhel, F. H. Gjorup, M. Klove, K. Borup and B. B. Iversen, *Inorg. Chem.*, 2022, **61**, 8760–8766.
35 L. Krause, **https://github.com/LennardKrause/**, accessed 12-05-2025.
36 Bruker Corp., *SAINT+ Integration Engine Reference Version 8.38 A Bruker*, AXS Inc., 2012.
37 L. Krause, R. Herbst-Irmer, G. M. Sheldrick and D. Stalke, *J. Appl. Crystallogr.*, 2015, **48**, 3–10.
38 G. M. Sheldrick, *TWINABS*, Bruker, Madison, Wisconsin, 2012.
39 G. Sheldrick, *Acta Crystallogr., Sect. A*, 2008, **64**, 112–122.
40 G. Sheldrick, *Acta Crystallogr., Sect. A*, 2015, **71**, 3–8.
41 G. Sheldrick, *Acta Crystallogr., Sect. C:Struct. Chem.*, 2015, **71**, 3–8.
42 O. V. Dolomanov, L. J. Bourhis, R. J. Gildea, J. A. K. Howard and H. Puschmann, *J. Appl. Crystallogr.*, 2009, **42**, 339–341.
43 A. Cavalleri, C. Tóth, C. W. Siders, J. A. Squier, F. Ráksi, P. Forget and J. C. Kieffer, *Phys. Rev. Lett.*, 2001, **87**, 237401.
44 H. S. Choi, J. S. Ahn, J. H. Jung, T. W. Noh and D. H. Kim, *Phys. Rev. B:Condens. Matter Mater. Phys.*, 1996, **54**, 4621–4628.
45 H. W. Verleur, A. S. Barker and C. N. Berglund, *Phys. Rev.*, 1968, **172**, 788.
46 G. Andersson, *Acta Chem. Scand.*, 1956, **10**, 623–628.
47 D. B. Mcwhan, M. Marezio, J. P. Remeika and P. D. Dernier, *Phys. Rev. B*, 1974, **10**, 490–495.
48 M. Marezio, B. Mcwhan, P. D. Dernier and J. P. Remeika, *Phys. Rev. B: Solid State*, 1972, **5**, 2541.
49 R. Ketkaew, Y. Tantirungrotechai, P. Harding, G. Chastanet, P. Guionneau, M. Marchivie and D. J. Harding, *Dalton Trans.*, 2021, **50**, 1086–1096.
50 M. A. Davenport, M. J. Krogstad, L. M. Whitt, C. W. Hu, T. C. Douglas, N. Ni, S. Rosenkranz, R. Osborn and J. M. Allred, *Phys. Rev. Lett.*, 2021, **127**, 125501.
51 J. M. Longo and P. Kierkega, *Acta Chem. Scand.*, 1970, **24**, 420.
52 Z. Hiroi, *Prog. Solid State Chem.*, 2015, **43**, 47–69.
53 M. Pan, J. Liu, H. M. Zhong, S. W. Wang, Z. F. Li, X. H. Chen and W. Lu, *J. Cryst. Growth*, 2004, **268**, 178–183.
54 A. O. Suleiman, S. Mansouri, N. Émond, B. Le Drogoff, T. Bégin, J. Margot and M. Chaker, *Sci. Rep.*, 2021, **11**, 1620.
55 (*a*) J. Svane, M. A. Quintero, E. S. Vosegaard, M. Kløve, D. A. Mayoh, G. Balakrishnan and B. B. Iversen, CCDC 2440825: Experimental Crystal Structure Determination, 2025, DOI: **10.5517/ccdc.csd.cc2mxw9r**.; (*b*) J. Svane, M. A. Quintero, E. S. Vosegaard, M. Kløve, D. A. Mayoh, G. Balakrishnan and B. B. Iversen, CCDC 2440826: Experimental Crystal Structure Determination, 2025, DOI: **10.5517/ccdc.csd.cc2mxwbs**; (*c*) J. Svane, M. A. Quintero, E. S. Vosegaard, M. Kløve, D. A. Mayoh, G. Balakrishnan and B. B. Iversen, CCDC 2440827: Experimental Crystal Structure Determination, 2025, DOI: **10.5517/**

ccdc.csd.cc2mxwct; (*d*) J. Svane, M. A. Quintero, E. S. Vosegaard, M. Kløve, D. A. Mayoh, G. Balakrishnan and B. B. Iversen, CCDC 2440828: Experimental Crystal Structure Determination, 2025, DOI: **10.5517/ccdc.csd.cc2mxwdv**; (*e*) J. Svane, M. A. Quintero, E. S. Vosegaard, M. Kløve, D. A. Mayoh, G. Balakrishnan and B. B. Iversen, CCDC 2440829: Experimental Crystal Structure Determination, 2025, DOI: **10.5517/ccdc.csd.cc2mxwfw**; (*f*) J. Svane, M. A. Quintero, E. S. Vosegaard, M. Kløve, D. A. Mayoh, G. Balakrishnan and B. B. Iversen, CCDC 2440830: Experimental Crystal Structure Determination, 2025, DOI: **10.5517/ccdc.csd.cc2mxwgx**; (*g*) J. Svane, M. A. Quintero, E. S. Vosegaard, M. Kløve, D. A. Mayoh, G. Balakrishnan and B. B. Iversen, CCDC 2440831: Experimental Crystal Structure Determination, 2025, DOI: **10.5517/ccdc.csd.cc2mxwhy**; (*h*) J. Svane, M. A. Quintero, E. S. Vosegaard, M. Kløve, D. A. Mayoh, G. Balakrishnan and B. B. Iversen, CCDC 2440832: Experimental Crystal Structure Determination, 2025, DOI: **10.5517/ccdc.csd.cc2mxwjz**; (*i*) J. Svane, M. A. Quintero, E. S. Vosegaard, M. Kløve, D. A. Mayoh, G. Balakrishnan and B. B. Iversen, CCDC 2440833: Experimental Crystal Structure Determination, 2025, DOI: **10.5517/ccdc.csd.cc2mxwk0**; (*j*) J. Svane, M. A. Quintero, E. S. Vosegaard, M. Kløve, D. A. Mayoh, G. Balakrishnan and B. B. Iversen, CCDC 2440834: Experimental Crystal Structure Determination, 2025, DOI: **10.5517/ccdc.csd.cc2mxwl1**; (*k*) J. Svane, M. A. Quintero, E. S. Vosegaard, M. Kløve, D. A. Mayoh, G. Balakrishnan and B. B. Iversen, CCDC 2440835: Experimental Crystal Structure Determination, 2025, DOI: **10.5517/ccdc.csd.cc2mxwm2**; (*l*) J. Svane, M. A. Quintero, E. S. Vosegaard, M. Kløve, D. A. Mayoh, G. Balakrishnan and B. B. Iversen, CCDC 2440836: Experimental Crystal Structure Determination, 2025, DOI: **10.5517/ccdc.csd.cc2mxwn3**; (*m*) J. Svane, M. A. Quintero, E. S. Vosegaard, M. Kløve, D. A. Mayoh, G. Balakrishnan and B. B. Iversen, CCDC 2440837: Experimental Crystal Structure Determination, 2025, DOI: **10.5517/ccdc.csd.cc2mxwp4**.